Integrating Materials and Manufacturing Innovation
https://doi.org/10.1007/s40192-025-00422-5

TECHNICAL ARTICLE

Automatic and Rapid Measurement in Artificial Intelligence-Aided Microstructure Analysis: A Deep Learning Approach Applied to AlSi9 Alloys

Mahmut Furkan Kalkan[1] · İbrahim Halil Kalkan[2] · Necip Fazıl Yilmaz[1,3] · Derya Dispinar[4] · Cem Kahruman[5] · Abdulcabbar Yavuz[6]

Received: 21 July 2025 / Accepted: 3 September 2025

Abstract
This study showcases a proof-of-concept of an artificial intelligence-driven analytical technique that facilitates the automated extraction of significant quantitative data from microstructural images. Semantic segmentation and classification were conducted on eutectic Si particles and dendritic architectures utilizing microscopic images of AlSi9 alloys with varying Sr ratios. Following segmentation, characteristics including area, aspect ratio, maximum Feret diameter, circularity and SDAS were assessed automatically, and the resulting values were compared with both literature and manual measurements. The samples were effectively categorized based on their alteration levels using a CNN-based classification algorithm. This technology provides significant temporal and financial benefits for microstructural investigation by executing the entire procedure autonomously and expeditiously. The minimal error rates and elevated accuracy findings demonstrate the usefulness and dependability of the devised method for automated microstructural analysis. This paper exemplifies the application of artificial intelligence-driven microstructural analysis techniques in materials science, addressing a significant gap in the literature.

Keywords Aluminum silicon alloy · Deep learning · Semantic segmentation · CNN · Microstructure analysis

Introduction

The evolution of metallic materials in industrial history, from the initial materials to contemporary advancements, has occupied a significant position. Speeding up the increment of the technology and the new subjects of life requirements have emerged the vitality of the enhancing material properties in many ways. Despite the development of numerous characterization techniques to describe metallic material properties, microstructural analysis and observation remain prevalent [1]. One of the crucial reasons of this prevalence of the microstructural examination could be stated as its close relationship between the physical, mechanical and chemical properties. The relationship between microstructure and other characteristics is crucial for understanding and creating new metallic materials [2]. The type, size, distribution and morphology of phases and intermetallic particles within the microstructure provide critical insights into the materials science tetrahedron (MST), serving as fundamental parameters in experimental materials research [3].

Advancements in microscopic characterization techniques have facilitated the quantitative and qualitative study of microstructural details. However, still there analyzing of microstructures has some confinement which conventionally microscopic analysis may not be adequate to provide full-fledged quantitative analyses with their accessory as hardware and software. This conditions results in an

✉ Mahmut Furkan Kalkan
mfkalkan@gantep.edu.tr

1 Department of Mechanical Engineering, Faculty of Engineering, Gaziantep University, 27310 Gaziantep, Türkiye

2 Daimler Truck AG, Leinfelden-Echterdingen, Germany

3 Board of Trustees, Hasan Kalyoncu University, 27010 Gaziantep, Türkiye

4 SINTEF Industry, Metal Production and Processing, 7034 Trondheim, Norway

5 Department of Metallurgical and Materials Engineering, Bursa Technical University, Bursa, Türkiye

6 Department of Metallurgical and Materials Engineering, Faculty of Engineering, Gaziantep University, 27310 Gaziantep, Türkiye

Published online: 18 September 2025

understanding of relations between the boundaries of MST with a lack of information [4]. The significance of quantitative outputs has risen, particularly following the advent of contemporary microscopic equipment that yield results with exceptional image quality. An improvement pace also has been continued via opportunity of modern technology in microstructural measurement over the last two decades. However, obtaining a remarkable microstructural image and analyzing the microscopic features required additional time, cost and expertise in many reasons [5].

Machine learning approaches provide a wide inspiration on automated and easier extraction of the characteristic feature from the microstructures. In fact, artificial intelligence tools technologies and approaches could already be seen in many industrial and academic areas such as food, medical, chemistry and other engineering disciplines with very impressive fare [6–8]. It was not long after artificial intelligence tools were first used in material science for microstructural characterization. First image processes were implemented on microstructures to characterize quantitatively. Tiley et al. [9] applied a thresholding and other image processing techniques to determine grain size and volume fraction in the titanium alloy microstructures. In one of the pioneering studies, Albuquerque et al. [10] successfully determined the graphite and pearlite phase fractions in cast iron microstructures by means of a neural network-based segmentation model. Recently, semantic segmentation models have led the microstructural studies in order to illustrate the potential of classification and feature extraction processes in metallic materials microstructures [11, 12].

With the increasing impact of deep learning in the last two decades, convolutional neural networks (CNNs) have emerged as powerful tools in microstructural analysis as well as in other fields in recent years, providing robust and high-throughput feature extraction. Deep learning-based approaches offer the ability to identify and segment complex microstructural patterns that are superior in accuracy and adaptability to traditional image processing and artificial intelligence techniques. For instance, Kalkan et al. [13] focused on comparative study in which discriminate the microstructural images of different AlSi alloy microstructures. Zhao et al. [14] proposed a CNN-based semantic segmentation model for the extraction of features such as grain number, average width, perimeter and area from the titanium microstructure. These ongoing studies are laying keystones in pursuit of automatic quantitative microstructural analysis [15]. Preprocessing [14, 16] and post-processing [17, 18] applications also indispensable factors to soar prediction of the machine learning and deep learning models.

This study presents a case in which features are automatically extracted from the microstructures of Al–Si alloys containing different strontium (Sr) percentages. The potential effects of rare earth elements on the chemical composition and microstructure of Al–Si alloys have been extensively examined in the literature [19–21]. The primary objective of this study is to propose an automated feature extraction methodology that integrates deep learning and image processing techniques for quantitative microstructural analysis. With the different ratio of Sr added in the chemical composition of casted AlSi alloy specimens were distinguished depend on quantitative analysis from microstructures.

Materials and Methods

AlSi9 alloy ingots that are available for purchase were divided into smaller fragments. Small quantities of Sr element, ranging from 100 to 500 ppm, were introduced into SiC at a furnace temperature of 750 °C. After undergoing 30 min of agitation at the designated temperature, the casting procedure was finalized by transferring the mixture into a steel mold with dimensions of 190 mm in length, 10 mm in thickness and 30 mm in width. A total of five specimens were prepared, including one pure AlSi9 alloy sample and five modified samples with Sr additions of 100, 200, 300, 500 ppm. The Sr concentrations were chosen to represent AlSi modification levels from 1 to 5, respectively [19]. Produced specimens and their chemical compositions, which were obtained from optical emission microscope, are presented in Table 1. A microscopic sample preparation procedure was conducted for all samples. All specimens were prepared for the grinding process with appropriate geometrical shapes. SiC emery papers with mesh sizes of 300, 600, 1000 and 1800 were utilized for grinding operations conducted underwater. The polishing processes were conducted using 1 µm Al_2O_3. The specimens were examined using a Nikon LV150N optical microscope, and images were

Table 1 Chemical contents of samples

Case Name	Si (%)	Sr (%)	Cu (%)	Mg (%)	Mn (%)	Fe(%)
0ppm Sr	9.72	–	0.002	0.003	0.001	0.001
100ppm Sr	9.72	0.01	0.01	0.001	0.001	0.31
200ppm Sr	8.86	0.02	0.02	0.002	0.006	0.32
300ppm Sr	8.5	0.03	0.01	0.001	0.001	0.28
500ppm Sr	9.21	0.05	–	–	0.004	0.22

captured using ToupTek ToupView software to observe their microstructure.

The microstructural images of modified and unmodified AlSi9 alloys were subjected to semantic segmentation using a fully convolutional network (FCN) architecture. Acquired images from the present work and hypoeutectic images from the literature [22–24] were used with an image size of 256 × 256 pixel during the training of FCN-based CNN model. TensorFlow was utilized as the framework of the model. Batch size was set as 16. All training and evaluating procedures were executed on Google Colab environment.

For the semantic segmentation operations to perform successfully, the dataset was divided into two. The model developed with the FCN architecture was trained separately with these datasets. One of the trainings was provided with 5 × magnification images where the secondary dendrite arm spacing (SDAS) measurement was performed, while the other was trained with microscopic images with 50 × magnification, to measure the aspect ratio, max. Feret diameter, circularity and average area parameters of the silicon particles in the microstructure. The training and validation results of the two models, which can be deemed to exhibit satisfactory metric performance, are shown in Table 2. To determine the error rates for the specified models, independent dendritic regions were utilized to calculate the average error rate at 5 × magnification, resulting in an error rate of 3.376% across 100 distinct dendritic regions. On the other hand, for the average error rate calculation at 50 × magnification, the average areas of independent Si particles were used, yielding an error rate of 4.762% for 100 different Si particles.

Microscopic images obtained at 5 × and 50 × magnifications were utilized for this process. SDAS (secondary dendrite arm spacing) measurements were automatically derived from the segmented images captured at 5 × magnification. Meanwhile, in the images taken at 50 × magnification, geometric properties such as the areas and aspect ratios of Si particles were automatically quantified. To address the challenges posed by the large pixel sizes in high-resolution microscopic images, the semantic segmentation models were applied to smaller sections of the images. These sections were processed individually, and the resulting black-and-white segmented images were then reassembled like a puzzle to form the full image; overall illustration of the processes is illustrated in Fig. 1. This approach allowed for successful segmentation and analysis while circumventing hardware limitations commonly encountered in microscopic applications. This methodology demonstrates the potential of using segmentation-based techniques to automate microstructural analysis in material science research, enhancing both precision and efficiency.

In addition to the FCN-based segmentation models, a deep learning model based on the DenseNet201 architecture was developed to classify the microstructural modification levels of AlSi9 alloys in accordance with the American Foundry Society (AFS) classification. The alloy specimens, which contained 0, 100, 200, 300 and 500 ppm of Sr element, were classified into five distinct modification levels, defined as Level 1 through Level 5, respectively. The assignment of the modification levels for the specimens was guided by the AFS classification system and supported by studies reported in the literature concerning Sr-containing Al–Si alloys. CNN-based classification model was trained using microscopic images taken from 20 × magnification, arbitrary cropped 180 × 180 pixel images from the originals. 383 original images and 82 original images were used for training and validation during the data augmentation processes. The training and validation steps were executed in Google Colab for 50 epochs where each training batch was composed of 16 images. In order to provide robust training for the classification of modification levels, fully connected layers, ReLU activation functions and dropout regularization were added to the structure of the DenseNet201 architecture. Accuracy and loss results from training and validation steps for provided classification model are also depicted in Table 2. The evaluation outcomes of the three models indicated that their performance was adequate for deployment in their respective classification and segmentation tasks.

Results and Discussion

The test results from provided models for three intended tasks are given in Table 3. The number of tested images depicted in Table 3 was deliberately selected to ensure a sufficiently representative evaluation for each model. FCN-based models, developed for carried out semantic

Table 2 Training performance results of provided models

Model	Mag	Image size	Training accuracy	Training loss	Validation accuracy	Validation loss
FCN (Segmentation for Si particles)	5x	256 × 256	0.9462	0.0102	0.9183	0.0165
FCN (Segmentation for dendrites)	50x	512 × 512	0.9562	0.0132	0.9163	0.0244
DenseNet201 (Modification level classification)	20x	180 × 180	0.9141	0.2274	0.8875	0.2314

Accuracy for FCN: Pixel Accuracy, Accuracy for DenseNet201: Test Accuracy

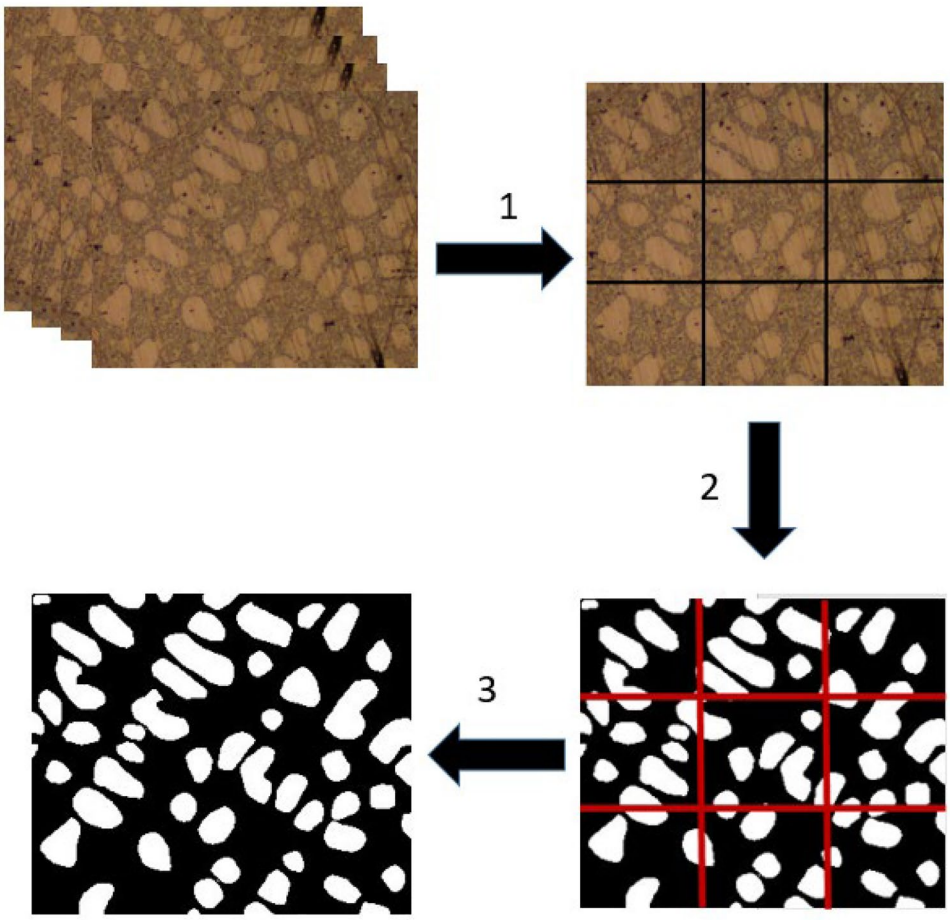

Fig. 1 Workflow of feature extraction through semantic segmentation

Table 3 Model performances in microstructural segmentation and classification tasks

Model	Tested image number	Accuracy	Precision	Recall	F1-score
FCN (Segmentation for Si particles)	120	95.53	93.36	92.22	92.79
FCN (Segmentation for dendrites)	60	95.46	92.64	92.38	92.48
DenseNet201 (Modification level classification)	120	91.67	92.36	91.67	91.69

segmentation process, attained high performance with F1-scores of 92.79% for Si particles and 92.48% for dendritic structures. It was indicated that the suggested models were overtly suitable for intricate and irregular morphologies in microstructural views from these results and other obtained valuable responses [25]. The DenseNet201 model attained an F1-score of 91.69% for classifying Sr modification levels, indicating its capability to effectively capture even minor visual transitions among the modification levels. Consistent performance across all models, with key metrics ranging from 91 to 96%, indicates that the models exhibit adequate generalization capability and resilience to microstructural variation, thereby affirming their potential for dependable and reproducible application in automated metallographic analysis [26].

Figure 2 shows microscopic images of samples at 50 × magnification with and without Sr added at different weight ratios, ranging from 0 to 500 ppm. The overall shape and distribution of the eutectic Si particles were characterized as coarse, elongated and randomly oriented from the unmodified microstructure which is given in Fig. 2. This definition could be used for first stage of the AFS modification scale [27]. There was sharp alteration was remarked under visual control with addition of 100 ppm Sr in the chemical composition of alloy. It was observed that with the added amount, the Si content in the coarse and elongated

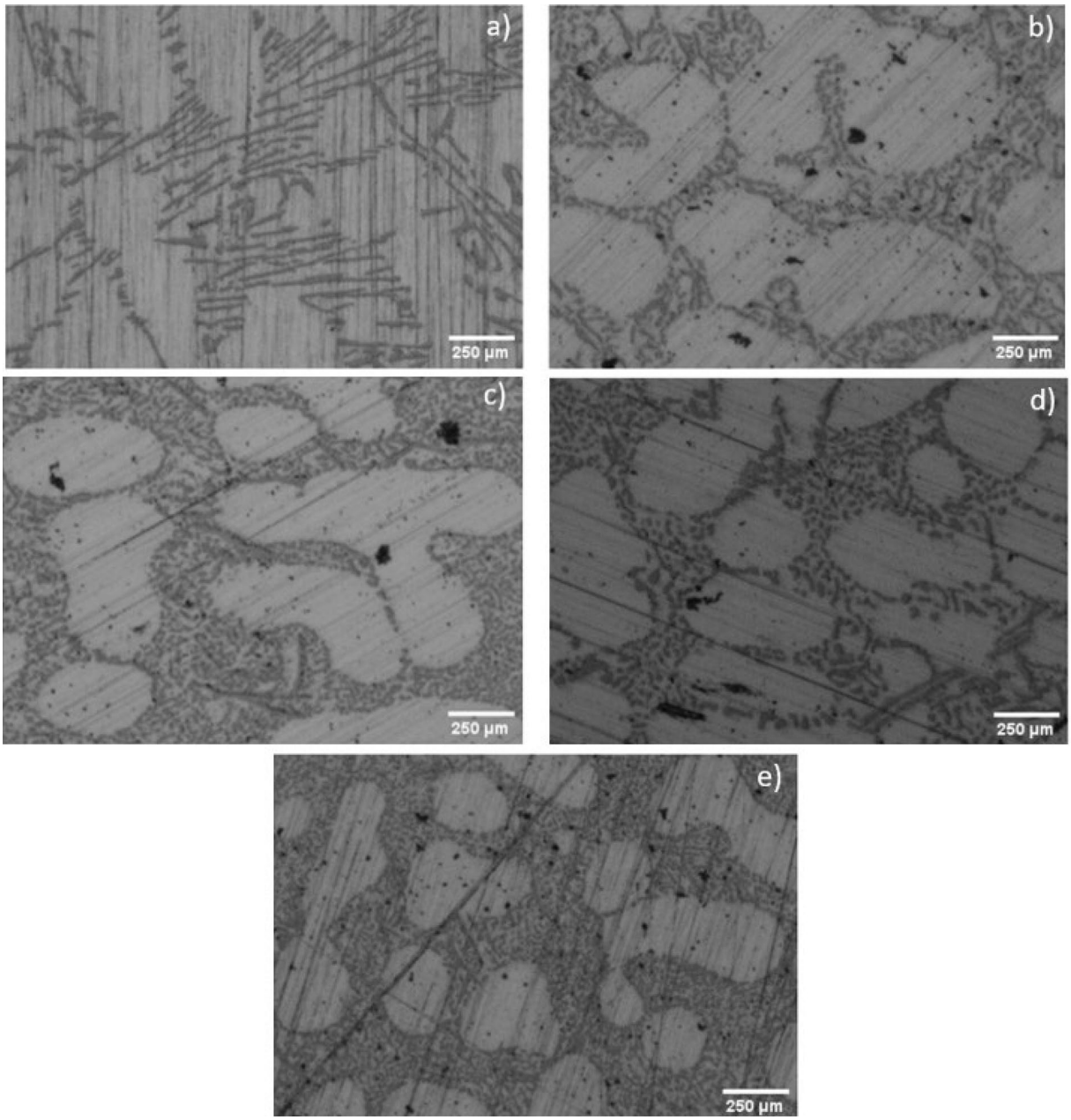

Fig. 2 Microstructural evolution of AlSi alloys with varying Sr additions at 50x: **a** 0 ppm, **b** 100 ppm, **c** 200 ppm, **d** 300 ppm, **e** 500 ppm

structure was replaced by a clearly modified Si content. The literature indicates that the addition of 100 ppm (Fig. 2b) Sr can significantly alter the microstructure, as demonstrated here [28]. With increasing of Sr content from 100 to 300 ppm (Fig. 2b–d), a continuous progression in morphological changes was observed, especially in Sr added samples at 200 ppm and 300 ppm, visually obtained a more round and smaller morphological characteristics of eutectic Si particles. This trend is ascribed to the influence of Sr on the kinetics of eutectic Si growth, which fosters multiple nucleation sites and hinders directional growth, thereby improving the spheroidization and refinement of the Si phase [29]. At 500 ppm Sr addition in the alloy content as seen in Fig. 2e, dramatically morphological change was seen from the unmodified microstructure. This is the stage at which the eutectic Si is observed as fine, uniformly dispersed particles that are highly branched. It was observed that as the amount of Sr increased, the number of primary Si needles increased became smaller and denser. It is a known fact in the literature that rare earth elements can cause such an effect when added in small amounts during casting. In addition, the position of different Sr ratios within the officially published

modification levels of AFS in microscopic images has been reported. It is stated that the AlSi alloy without Sr added has a 1st level modification level, and when 100, 200 and 300 ppm are added, it has a 2nd, 3rd and 4th level modification level, respectively. It was noted that at 500 ppm, it reached the 5th modification level, which is stated as the final level [30].

Although qualitative interpretations could be made based on the microscopic images presented in the literature, such evaluations may not always be adequate in cases where quantitative analysis is essential and where microscopic data should be interpreted in a meaningful and measurable manner. In this context, it is considered that microscopic images could be utilized more effectively through image processing techniques integrated with machine learning and deep learning, allowing for faster and more practical quantitative analysis. In the scope of the indication of the performance for proposed method, Fig. 3a is given to illustrate the performance of the Sr addition on average particle area of silicon. Areal change of the silicon particles in the microstructures was detected obviously with respect to addition of the Sr element in weight. 17.73 μm^2 was found from the microstructural images of unmodified AlSi alloy by Sr. 36.83% reduction was observed in the average particle area with the addition of Sr with 100 ppm. It was observed that these decreases continued until the AlSi alloy with 500 ppm added. In the AlSi alloy with 500 ppm added, an average Si particle area of 92.78%, which was the largest decrease among the produced samples, was seen as 1.28 μm^2. A comprehensive change of the maximum Feret diameter the silicon particles in microstructures are distributed in Fig. 3b. It was determined that the AlSi microstructure was not modified with Sr had a significant average Feret diameter compared to other samples. In the sample modified with 500 ppm Sr, it was observed that the maximum Feret diameter decreased by 86.78%. It was observed that the sharpest decrease in Feret diameter undoubtedly occurred when 100 ppm was added, and in subsequent samples, there was a decrease in the average maximum Feret diameter at slightly smaller scales. Nearly same trend which representing the diminishing of average area and max. Feret diameter values was indicated from these figures. According to these graphs, the sharpest decrease in these values was obtained from after 100 ppm Sr added and secondly 200 ppm Sr added specimens. The literature indicates

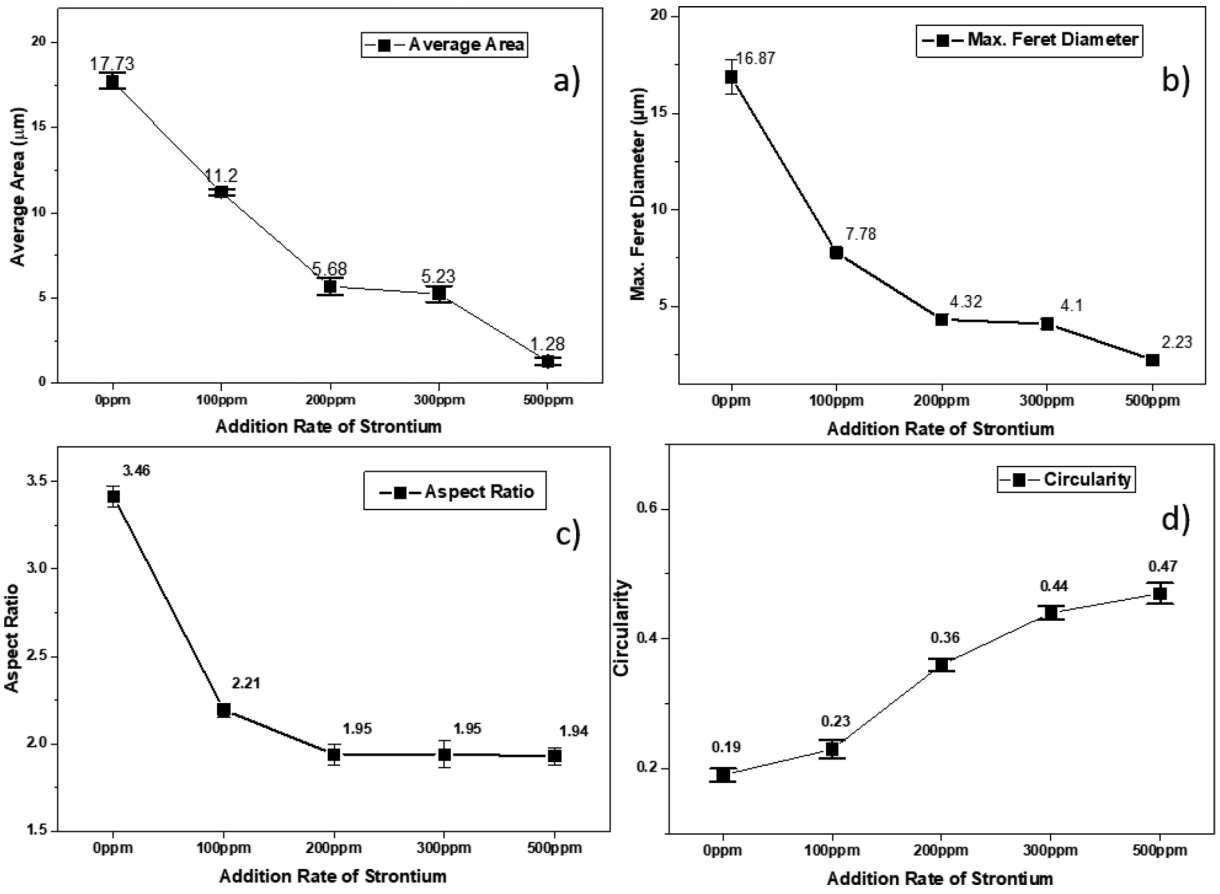

Fig. 3 Effect of strontium addition on morphological characteristics of eutectic silicon: **a** average area, **b** maximum Feret diameter, **c** aspect ratio, and **d** circularity

that the nucleation rate markedly increases in alloys containing 100–200 ppm Sr, whereas this increase remained mild in alloys with higher Sr concentrations [31]. Consequently, it was logical that the Si particles in samples with Sr additions exceeding 200 ppm display analogous values in their microstructural parameters [32].

Aspect ratio results are given in Fig. 3c, and the trend from the obtained results is remarked it resemblance to average area and max. Feret diameter, as expected. In the ratio measurement results, it was seen that there was a difference of 43.93% between AlSi modified with 500 ppm Sr and unmodified AlSi. It was observed that the biggest change was again in the sample with 100 ppm Sr added. At later levels, it was determined that there was a much lower aspect ratio change. It was seen that the only part where the trend changed between the two quantitative measurements was in the AlSi alloy with 500 ppm Sr added. Notably, it was seen that 3 specimens, which have 200 ppm, 300 ppm and 500 ppm Sr content in the alloy, acquired close values from Fig. 3c. It was thought that the observation of this situation despite the decreasing effect of the Feret diameter might be related to the spherization of the particles. Alteration of the circularity results from the microstructural images is indicated in Fig. 3d. Circularity of the silicon particle in microstructure of unmodified AlSi alloy was found as 0.19. The level of the circularity for this alloy was expected because of the overall shape of the silicon parts in Fig. 2b. The trend of this quantitative measurement results was detected different from the other measurements. There was no significant change in circularity between the unmodified and modified 100 ppm Sr AlSi alloys, in contrast to the average area, aspect ratio and maximum Feret diameter. In this case, it was thought that although the size and aspect ratio of the Si particles in the AlSi alloy modified with 100 ppm Sr decreased, the structure remained in a fibrous structure. As the Sr ratio increased, it was observed that this fibrous structure gradually became rounder at 200 ppm and later levels. In Fig. 3a despite the rise in Feret diameter, the reduction in aspect ratio was considered consistent with this scenario [33]. The findings indicate that the Sr element influences both particle size and particle geometry in the morphological evolution of the alloy structure [34]. The low error rates of the developed method confirm that the roundness of eutectic Si significantly improves beginning at 200 ppm Sr, as evidenced by aspect ratio and circularity measurements.

To illustrate the dendritic phases of the AlSi alloy specimens, microscopic images taken at 5 × magnification using a 5 × objective lens are provided in Fig. 4. By qualitatively analyzing the microscopic images, changes affecting the dendrite phase were detected. To provide a certain objective measurement standard for all samples, quantitative measurements were made in an area of 11.63 mm2 using 5 × magnification. This approach was adopted to enhance the accuracy and comparability of microscopic measurements. The change of the morphology is quietly acknowledged by analyzed these microimages visually. The inclusion of 100 ppm Sr into the alloy was found to cause a partially discernible modification in the image presented in Fig. 4b. It is known from previous studies that even if the modification occurs as a result of adding 100 ppm, the Sr element will not cause a significant visual difference, especially in a microimage at this magnification, after adding this amount [35, 36]. The obtained microstructural images were taken from the alloys with 200 and 300 ppm Sr additions in their chemical content. The images in Fig. 4c and d, resulting from the addition of 200 and 300 ppm Sr, respectively, visually demonstrate a distinct modification compared to the alloy without Sr incorporation. It was concluded that no substantial visual disparity existed between the microstructures of the two samples. In the alloy in Fig. 4e containing 500 ppm Sr in its chemical content, it was observed that the dendritic arms became significantly thinner compared to the other samples and the number of independent structures increased in the determined area. Such morphological changes, observed in Fig. 2 due to addition of Sr content, will also effect the microstructure in macro view [37]. Although general morphological differences are visually apparent in the micrographs, discerning subtle variations among all samples can be difficult. This underscores the prospective function of image-based artificial intelligence techniques in materials science. These technologies are anticipated to aid in detecting nuanced variations in microstructural morphology that are not easily discernible through traditional visual inspection [38].

The secondary dendrite arm spacing (SDAS) and dendritic area fraction in AlSi alloys are influenced by varying strontium (Sr) additives, as illustrated in Fig. 5. The most remarkable refinement in dendritic structure was observed at 500 ppm, as demonstrated by the microstructural images and the SDAS data in Fig. 5a, out of the five Sr addition levels that were tested. SDAS is one of the metrics that can be used to understand the modification in the dendritic mechanism. It is given to show the SDAS values calculated from the microscopic images of samples produced under different conditions. While an average value of 34.99 mm was observed in the original AlSi alloy, it was observed that this value partially decreased when 100, 200 and 300 ppm Sr was added. The observed refinement in the SDAS especially in 500 ppm Sr added specimen could be grounded on the altered nucleation and growth behavior of the dendrites. According to Vasudevan et al. [39], Sr additions enhance the uniformity of the nucleation front and impede solute redistribution, hence mitigating dendritic coarsening. Furthermore, the segregation of Sr near the solidification front induces localized undercooling, hence promoting the fragmentation and branching of dendritic arms.

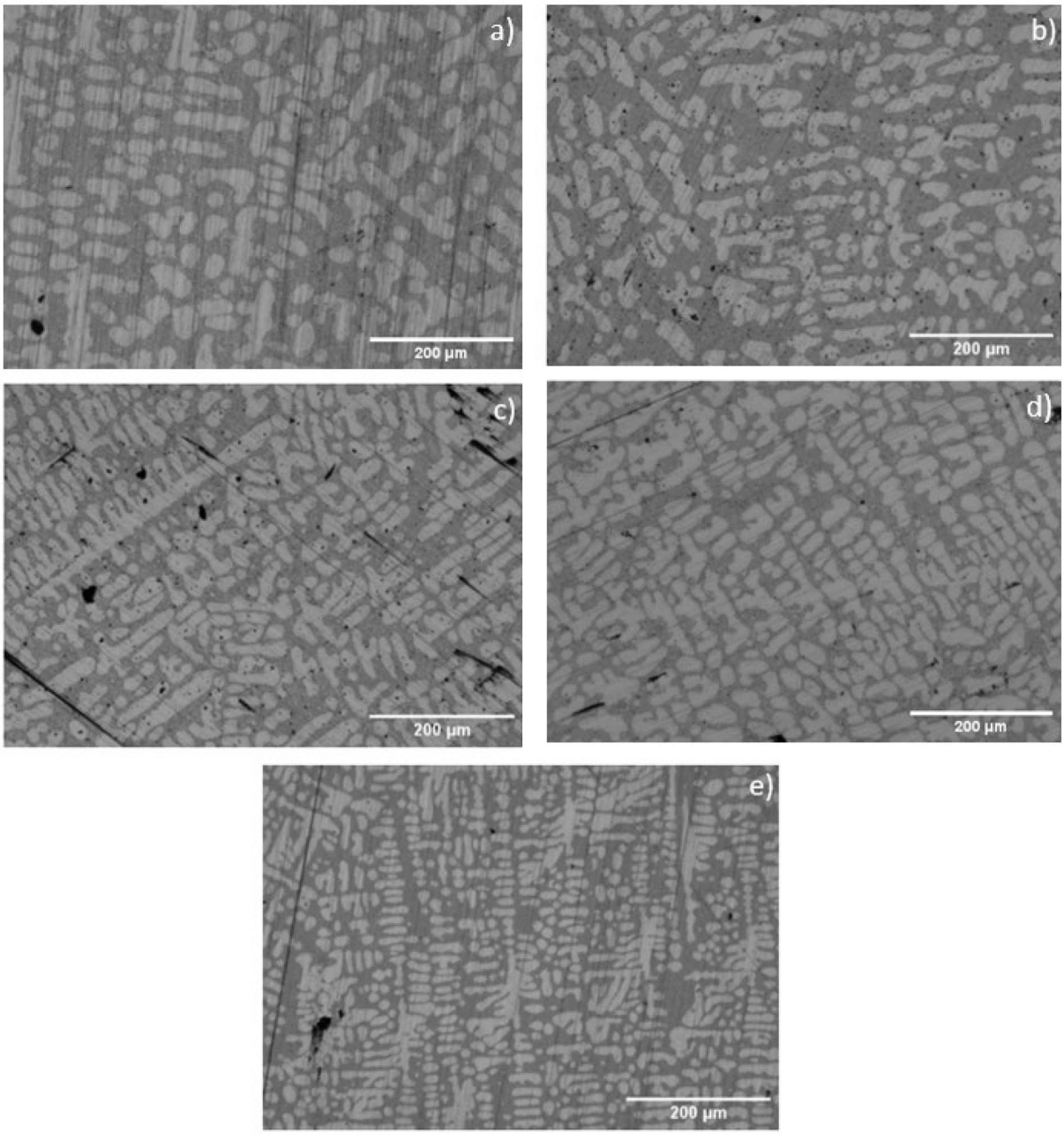

Fig. 4 Microstructural evolution of AlSi alloys with varying Sr additions at 5x: **a** 0 ppm, **b** 100 ppm, **c** 200 ppm, **d** 300 ppm, **e** 500 ppm

The comprehensive graph for the areal fraction of the dendrite areas is given in Fig. 5b. It was observed that there was no serious areal fraction change in the dendrite region calculated from the microscopic images of unmodified AlSi alloys modified by adding 0 ppm and 100 ppm Sr. It was determined that there was a significant difference in the AlSi alloy produced with 300 ppm Sr reinforcement compared to these three alloys. The areal fraction value of the dendrite region, which is around 40%, was calculated as 48.29%. It was thought that this result could be due to the cooling effect during casting rather than the measurement error made on the sample produced. It was observed that the areal fraction decreased in 500 reinforced AlSi alloys where the Sr amount was higher. It was observed that the AlSi alloy with 500 ppm Sr added had a slightly higher areal fraction than the AlSi alloys with 0, 100 and 200 ppm added. This unexpected change of the areal fraction in could suggest that the dendritic area fraction is not solely determined by the Sr content but is also influenced

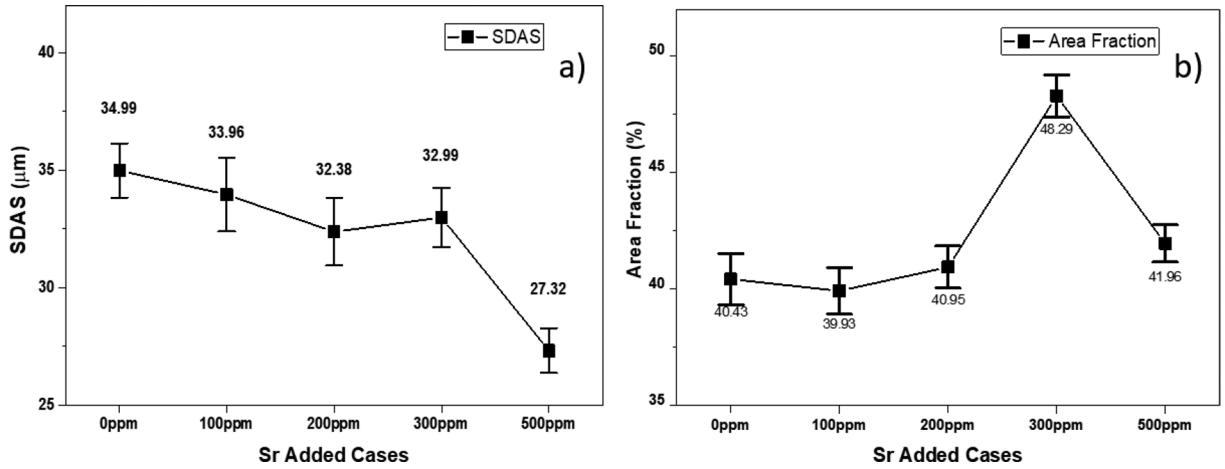

Fig. 5 Effect of strontium addition on morphological characteristics of eutectic silicon: **a** SDAS, **b** area fraction of dendritic phase

by external solidification conditions, such as cooling rate, thermal gradients and melt flow during casting [21, 34].

The outcomes derived from the two models created for photos captured at 5 × and 50 × magnifications are presented in Figs. 3 and 5. To validate the dependability of the results in these two figures, manual measurements were conducted on manually selected samples and thereafter compared with the outcomes of the devised approach. This comparison involved measurements of 100 separate silicon particles in photos captured at 5 × magnification. The SDAS and area fraction characteristics were measured on 30 sample pictures, each consisting of regions of 256 × 256 pixels, captured at 50 × magnification. The error rates resulting from these techniques are presented in Fig. 6. The observed error rates ranged between 4 and 8%, with the highest values identified in the measurements of area fraction and circularity. Despite these deviations, the developed method was considered to produce consistent and reliable results for the given dataset.

Average area, max. Feret diameter, aspect ratio and circularity results for Si particles automatically measured with the method developed from the microstructure and Pearson's correlation coefficients of SDAS and area fraction results measured from the dendritic image depending on the amount of Sr by weight in the alloy are given in Table 4. The Sr rate exhibited a significant negative connection with the average area (r = –0.912) and maximum Feret diameter (r = –0.815), implying that an increase in Sr concentration in the alloy markedly diminishes the size of Si particles. The aspect ratio exhibited a considerable negative connection with the Sr rate (r = –0.700), suggesting that increased Sr content is linked to diminished aspect ratios of Si particles. Circularity demonstrated a robust positive connection (r = 0.930) with Sr rate, indicating that elevated Sr levels are statistically associated

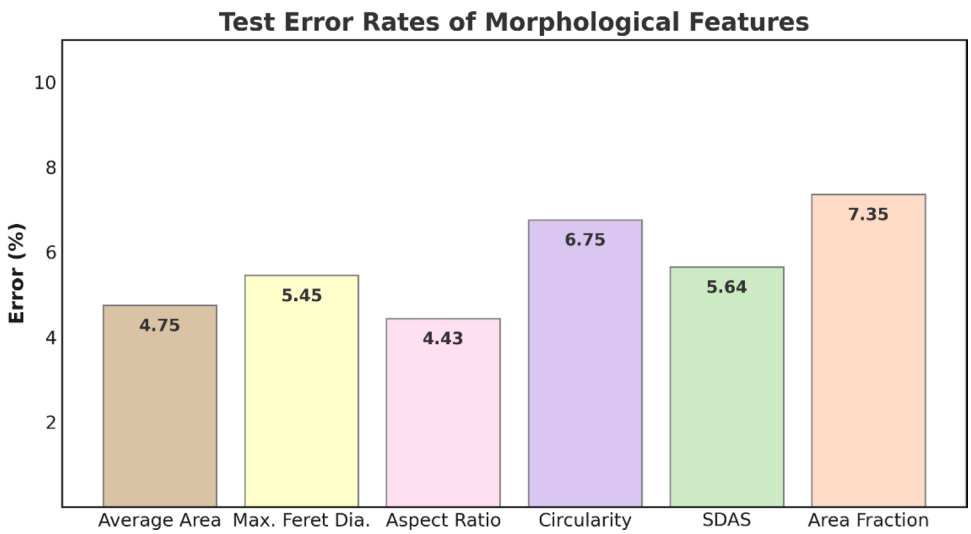

Fig. 6 Error rates of extracted microstructural features

Table 4 Pearson's correlation test (r values) between Sr rate and feature extracted responses from microstructure

	Sr. rate	Average area	Max. Feret dia	Aspect ratio	Circularity	SDAS	Area fraction
Sr. Rate	1						
Average area	−0.912	1					
Max. Feret dia	−0.815	0.971	1				
Aspect ratio	−0.700	0.901	0.978	1			
Circularity	0.930	−0.957	−0.883	−0.780	1		
SDAS	−0.897	0.859	0.752	0.616	−0.824	1	
Area fraction	−0.129	−0.069	−0.117	−0.132	0.190	0.164	1

with increasing circularity values. SDAS had a robust negative correlation with Sr (r = –0.897), although the correlation between Sr and area fraction was poor (r = –0.129), indicating minimal to no linear connection between these two variables. Moreover, based on Pearson's correlation results, area fraction also appeared to be weakly or negligibly associated with the other morphological descriptors, suggesting that it behaves independently from shape- and size-related parameters such as average area, max. Feret diameter, aspect ratio and circularity. These observations could be tough that consistent with previous studies showing the Sr or any other rare earth material induced modification sparks spheroidization of Si particles through poisoning of growth fronts [40, 41].

Classification test results are given in Fig. 7. The CNN model demonstrated high classification performance, particularly for the extreme modification levels. Level 1 (unmodified) and Level 5 (highly modified) were classified with strong accuracy, with 24/24 and 21/24 correct predictions, respectively. Misclassifications occurred predominantly between adjacent levels, such as Level 2 being confused with Level 3, and Level 5 with Level 4. This is consistent with the gradual nature of microstructural transitions across modification levels, where visual boundaries between adjacent classes may be more subtle. These results suggest that the model successfully captured the distinct features of highly separated classes, while finer differentiation between intermediate levels remains more challenging. This difficulty is thought to be primarily due to the increasing similarity of microstructures and their associated values in the mid-range levels, particularly as fine silicon morphologies begin to exhibit rounding. Despite these overlaps in appearance and quantitative indicators, the model's ability

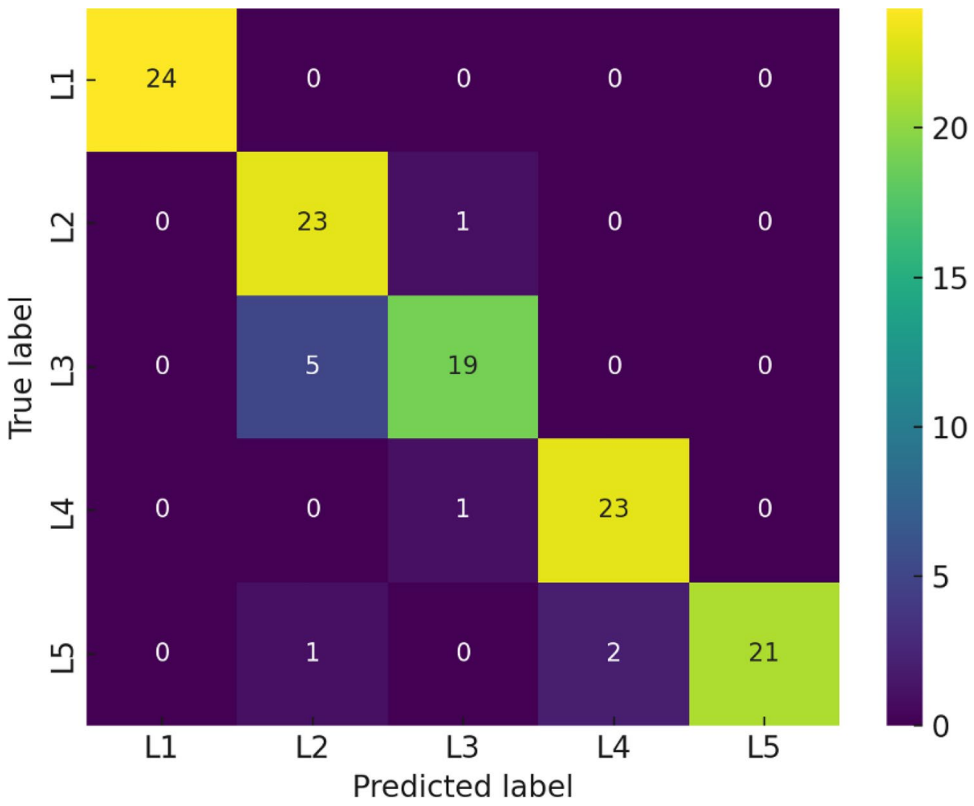

Fig. 7 Confusion matrix of CNN model for classification of five microstructural modification levels (L1–L5)

to maintain a reasonable classification performance across all levels indicates its suitability for practical applications. This observation is in line with recent studies where CNN-based models have been used for microstructural classification. Similar difficulties in adjacent-class prediction have been reported by DeCost et al. [42] and Azimi et al. [43], particularly in cases of metallic micromorphologies.

Conclusions

In this study, the classification, semantic segmentation and post-processing processes of automatic quantitative measurement methods developed for microstructural analysis of AlSi9 alloys were presented. Here, a comprehensive research decision was made using common structural models to be created in three steps to select suitable architectures. Necessary metrics were extracted in all steps, and the selection was made according to their results. After all steps, basic steps that could be measured quantitatively microscopically were measured and error rates were observed. Then, microscopic images of AlSi9 alloys produced under different conditions were subjected to automatic quantitative analysis with this developed method. The main contribution of this study is that this result obtained within the scope of the study was not made on a few Si particles taken from a small area, but instead, much more than the area that could be controlled by eye can be automatically scanned with a certain number of images and the trend could be shown. It should also be noted that this process is provided with small error rates. This study emphasizes how automatic microstructural analysis can improve material design and development and how it can fill the gap between data analysis and practical application.

Acknowledgements The authors thank the Scientific Research Project Unit at Gaziantep University (MF.DT.24.1).

Author Contributions M.F. Kalkan was involved in software development, formal analysis, data curation and writing—original draft. İ.H. Kalkan contributed to experimental design, sample preparation and data collection. N.F. Yılmaz contributed to supervision, methodology and writing—review and editing. A. Yavuz was involved in supervision, data interpretation and writing—review and editing. D. Dışpınar contributed to conceptualization and writing—review and editing. C. Kahruman helped with metallurgical interpretation and writing—review and editing.

Data Availability The codes required to reproduce these findings are available at https://github.com/mahmutfurkankalkan/AlSi-Alloy-Microstructures-with-Different-Sr-ratios-

Declarations

Conflict of interest The authors declare that they have no known competing financial interests or personal relationships that could have appeared to influence the work reported in this paper.

References

1. Kablov EN, Antipov VV, Oglodkova JS, Oglodkov MS (2021) Development and application prospects of aluminum–lithium alloys in aircraft and space technology. Metallurgist 65:72–81
2. Žbontar M, Petrič M, Mrvar P (2021) The influence of cooling rate on microstructure and mechanical properties of AlSi9Cu3. Metals (Basel) 11:186
3. Müller M, Stiefel M, Bachmann B-I, Britz D, Mücklich F (2024) Overview: machine learning for segmentation and classification of complex steel microstructures. Metals 14:553
4. Zhang J, Gao H, Liu Y, Wang J (2025) A review on the application of superalloys composition, microstructure, processing, and performance via machine learning. JOM 77:106–124
5. Kang J-Y, Park S-J, Suh D-W, Han HN (2013) Estimation of phase fraction in dual phase steel using microscopic characterizations and dilatometric analysis. Mater Charact 84:205–215
6. Kalkan E, Maskan M (2025) Optimizing production of gluten-free, sugar-reduced cupcakes: utilizing stevia as natural sweetener and psyllium as gluten substitute. J Food Sci 90:e70148
7. Younis HA, Eisa TAE, Nasser M, Sahib TM, Noor AA, Alyasiri OM et al (2024) A systematic review and meta-analysis of artificial intelligence tools in medicine and healthcare: applications, considerations, limitations, motivation and challenges. Diagnostics 14:109
8. Wang H, Fu T, Du Y, Gao W, Huang K, Liu Z et al (2023) Scientific discovery in the age of artificial intelligence. Nature 620:47–60
9. Tiley J, Searles T, Lee E, Kar S, Banerjee R, Russ JC et al (2004) Quantification of microstructural features in α/β titanium alloys. Mater Sci Eng A 372:191–198
10. de Albuquerque VHC, Cortez PC, de Alexandria AR, Tavares JMRS (2008) A new solution for automatic microstructures analysis from images based on a backpropagation artificial neural network. Nondestruct Test Eval 23:273–283
11. Kalkan MF, Aladag M, Kurzydlowski KJ, Yilmaz NF, Yavuz A (2024) A comprehensive comparative study on semantic segmentation for automated microstructural measurement in Al–Si alloys. J Mater Eng Perform. https://doi.org/10.1007/s11665-024-10442-5
12. Muñoz-Rodenas J, García-Sevilla F, Miguel-Eguía V, Coello-Sobrino J, Martínez-Martínez A (2024) A deep learning approach to semantic segmentation of steel microstructures. Appl Sci 14:2297
13. Kalkan MF, Aladag M, Kurzydlowski KJ, Yilmaz NF, Yavuz A (2024). Comparative study on different CNN architectures developed on microstructural classification in Al–Si alloys. Arch Metall Mater. 563–70
14. Zhao P, Wang Y, Jiang B, Wei M, Zhang H, Cheng X (2023) A new method for classifying and segmenting material microstructure based on machine learning. Mater Des 227:111775
15. Alrfou K, Zhao T, Kordijazi A (2024) Deep learning methods for microstructural image analysis: the state-of-the-art and future perspectives. Integr Mater Manuf Innov 13:703–731
16. De Raad KB, van Garderen KA, Smits M, van der Voort SR, Incekara F, Oei EHG, et al. (2021). The effect of preprocessing on convolutional neural networks for medical image segmentation. 2021 IEEE 18th Int. Symp. Biomed. Imaging, IEEE; 655–8
17. Fotos G, Campbell A, Murray P, Yakushina E (2023) Deep learning enhanced watershed for microstructural analysis using a boundary class semantic segmentation. J Mater Sci 58:14390–14410
18. Kalkan MF, Yavuz A, Yılmaz NF (2024). Refining microstructural analysis in metallurgy: semantic segmentation enhanced by post-processing. Turkish J Mater 9

19. Kalkan İH, Hızlı İG, Dizdar KC, Kahruman C, Dispinar D (2024) Statistical distribution of Si phases at different Sr levels in AlSi9 alloys. Metallogr Microstruct Anal 13:130–144
20. Ding W, Xu M, Gou L, Li L, Ma J, An J et al (2024) Refinement mechanism of the hypoeutectic Al–7Si alloy by adding a novel La-rich rare-earth grain refiner. Metall Mater Trans A 55:3617–3626
21. Faraji M, Katgerman L (2010) Distribution of trace elements in a modified and grain refined aluminium–silicon hypoeutectic alloy. Micron 41:554–559
22. Schmitz-Metallographie GmbH (2023). Microstructure Database. Available at: https://www.schmitz-metallographie.de/en/gefugedatenbank/al-base/. Accessed 20 August 2023
23. Pastirčák R, Brůna M, Bolibruchová D (2019). The influence of different wall thicknesses of the casting in the direct squeeze casting. Arch Foundry Eng. 19–24
24. A356-M, Innovation Project Metallographic Atlas. Universidad Complutense de Madrid. Available at: https://www.ucm.es/metallographicatlas/a356-m. Accessed 20 August 2023
25. Xie L, Li W, Fan L, Zhou M (2023) Automatic identification of the multiphase microstructures of steels based on ASPP-FCN. Steel Res Int 94:2200204
26. Na J, Kim S-J, Kim H, Kang S-H, Lee S (2023) A unified microstructure segmentation approach via human-in-the-loop machine learning. Acta Mater 255:119086
27. Apelian D, Sigworth GK, Whaler KR (1984) Assessment of grain refinement and modification of Al-Si foundry alloys by thermal analysis. AFS Trans 92:297–307
28. Ammar HR, Samuel E, Elsharkawi E, Doty HW, Songmene V, Samuel FH (2025). Effect of Be, Sr, Mn, Mg, Cr and Si Addition on Neutralization and Fragmentation of β-Al5SiFe Phase in Al-(6–10)% Si Alloys. Int J Met. 1–24
29. Ming X, Song D, Yu A, Tan H, Zhang Q, Zhang Z et al (2023) Effect of heat treatment on microstructure, mechanical and thermal properties of selective laser melted AlSi7Mg alloy. J Alloys Compd 945:169278
30. Radwan B (2020). Treatment of a liquid Al–Si alloy: quality control and comparison of two melt degassing processes
31. Doğdu B, Ertuğrul O, Aybarç U, Gündoğdu S (2021) Determination of the effect of cooling rate and Strontium amount on eutectic Si modification performance of A356 alloy via casting simulation. Celal Bayar Üniversitesi Fen Bilimleri Dergisi 17:275–283
32. McDonald SD, Nogita K, Dahle AK (2006) Eutectic grain size and strontium concentration in hypoeutectic aluminium–silicon alloys. J Alloys Compd 422:184–191
33. Zhang W, Ma S, Wei Z, Bai P (2019) The relationship between residual amount of Sr and morphology of eutectic Si phase in A356 alloy. Materials 12:3222
34. De Giovanni M, Kaduk JA, Srirangam P (2019) Modification of Al-Si alloys by Ce or Ce with Sr. JOM 71:426–434
35. Timpel M, Wanderka N, Schlesiger R, Yamamoto T, Isheim D, Schmitz G et al (2013) Sr–Al–Si co-segregated regions in eutectic Si phase of Sr-modified Al–10Si alloy. Ultramicroscopy 132:216–221
36. Nogita K, Yasuda H, Yoshida K, Uesugi K, Takeuchi A, Suzuki Y et al (2006) Determination of strontium segregation in modified hypoeutectic Al–Si alloy by micro X-ray fluorescence analysis. Scr Mater 55:787–790
37. Liao H, Sun Y, Sun G (2002) Correlation between mechanical properties and amount of dendritic α-Al phase in as-cast near-eutectic Al–11.6% Si alloys modified with strontium. Mater Sci Eng A 335:62–66
38. Maqsood A, Chen C, Jacobsson TJ (2024) The future of material scientists in an age of artificial intelligence. Adv Sci 11:2401401
39. Vasudevan G, Anbukkarasi R, Sanil H, Ravi M (2023) Combined effect of Sr-addition and pressure induced solidification on eutectic-Si morphology and mechanical properties of squeeze cast Al-Si binary alloy. Mater Today Commun 34:105104
40. Mao F, Liu S, He Y, Guo A, Wei S, Chen C et al (2025) Effect of rare earth Dy (dysprosium) on the microstructures and mechanical properties of hypereutectic Al–Si alloy. Int J Metalcast 19:1048–1066
41. Chong Y, Du Z, Gong T, Wang W, Pan Z, Qi L et al (2025) Microstructure and mechanical properties of Ce-La mixed rare earths modified Al-Mg-Si alloy under cold rolling and heat treatment. J Alloys Compd 1021:179773
42. DeCost BL, Francis T, Holm EA (2017) Exploring the microstructure manifold: image texture representations applied to ultrahigh carbon steel microstructures. Acta Mater 133:30–40
43. Azimi SM, Britz D, Engstler M, Fritz M, Mücklich F (2018) Advanced steel microstructural classification by deep learning methods. Sci Rep 8:2128